

## Theoretical and experimental study of the nitrogen-vacancy center in 4H-SiC

Yizhi Zhu and Berk Kovos 

*Pritzker School of Molecular Engineering, University of Chicago, Chicago, Illinois 60637, USA*

Mykyta Onizhuk

*Department of Chemistry, University of Chicago, Chicago, Illinois 60637, USA*

David Awschalom 

*Pritzker School of Molecular Engineering, University of Chicago, Chicago, Illinois 60637, USA;*

*Department of Physics, University of Chicago, Chicago, Illinois 60637, USA;*

*and Materials Science Division and Center for Molecular Engineering, Argonne National Laboratory, Lemont, Illinois 60439, USA*

Giulia Galli \*

*Pritzker School of Molecular Engineering, University of Chicago, Chicago, Illinois 60637, USA*

*Department of Chemistry, University of Chicago, Chicago, Illinois 60637, USA*

*and Materials Science Division and Center for Molecular Engineering, Argonne National Laboratory, Lemont, Illinois 60439, USA*



(Received 15 May 2021; accepted 9 July 2021; published 27 July 2021; corrected 29 July 2021)

Using first-principles calculations and magnetic resonance experiments, we investigated the physical properties of the negatively charged nitrogen-vacancy (NV) center in 4H-SiC, a promising spin qubit. Our predictive theoretical model in conjunction with experimental measurements reveals a large sensitivity to strain and symmetry. The measured and computed zero-phonon lines (ZPLs) are in agreement and show a consistent trend as a function of the defect location in the crystal. The computed ZPLs are extremely sensitive to the geometrical configurations of the ground and excited states, and large supercells with more than 2 000 atoms are required to obtain accurate numerical results. We find that the computed decoherence time of the basal NV centers at zero magnetic field is substantially larger than that of the axial configurations. Furthermore, at natural nuclear spin abundance and zero field, the Hahn-echo coherence time of one of the basal configurations is similar to that of the axial divacancy in isotopically purified SiC.

DOI: [10.1103/PhysRevMaterials.5.074602](https://doi.org/10.1103/PhysRevMaterials.5.074602)

### I. INTRODUCTION

Spin defects in wide-band-gap semiconductors have emerged as promising platforms for quantum information technologies [1,2]. The negatively charged nitrogen-vacancy (NV) center in diamond is one of the prototypical spin defects displaying the required properties [3,4] to realize a qubit, and it has been studied in depth over the last decades [5–7]. Point defects in SiC, notably divacancies, have also been extensively investigated and shown to exhibit many desired properties, including long coherence times [8–12]. Recently, the NV center in several polytypes of SiC [13–18] has drawn the attention of experimentalists and theorists alike. The substitutional nitrogen atom makes the defect complex easier to localize within a host material [19–22]; most importantly it provides an extra nuclear spin register, compared to, e.g., the divacancy, which can act as an extra degree of freedom for control and manipulation. Coherent control of NV ensembles in 4H-SiC has been reported, with spin dephasing time  $T_2^*$  of  $0.4 \mu\text{s}$  [23] and a room-temperature  $T_2$  of  $17.1 \mu\text{s}$  [24]. These findings point at the NV center in SiC as a possible candidate

for room-temperature quantum sensing applications. In addition, experiments have demonstrated that single NV centers in 4H-SiC have robust optical properties over a wide temperature range and they can act as single-photon sources, thus making them interesting platforms for quantum photonics [25].

However, some of the basic physical properties of NV centers in SiC are not fully understood. Contradictory experimental and theoretical results have been reported for the zero-phonon lines (ZPLs) of the NV in 6H- and 4H-SiC, as summarized in Table I. Different experiments and first-principles calculations are in disagreement on the ordering of the ZPL as a function of the defect configuration in the host material. Hybrid density functional theory (DFT) calculations appear to agree with early experimental results [26], which have, however, been later updated and modified [27]. Another theoretical study appears to be consistent with the more recent experimental trends; however, only vertical excitation energies (using both semilocal and hybrid DFT) instead of ZPLs were computed [27]. Similar discrepancies between theory and experiments have also been found in the characterization of the NV in 6H-SiC [18,28]. Measured and computed zero-field splitting values, summarized in Table II, are instead consistent with each other, albeit not in quantitative agreement [18,27].

\*Corresponding author: gagalli@uchicago.edu

TABLE I. Measured and computed zero-phonon lines (eV) of the NV center in 4H-SiC. In Ref. [18] calculations were carried out with cells of 576 atoms with the Heyd-Scuseria-Ernzerhof (HSE) functional. In Ref. [27] the authors used instead 768 atoms with PBE and HSE functionals (both shown) but reported vertical excitation energies (VEEs) as an approximation of ZPLs. Diff. (Expt./Theor.) is the difference between the results obtained in this work.

Configuration	Expt. <sup>a</sup>	Expt. <sup>b</sup>	Expt. <sup>c</sup>	Theor. <sup>d</sup>	Theor. <sup>b</sup> VEE	Theor. <sup>c</sup>	Diff. (Expt./Theor.)
hh	0.998	1.051	1.051	0.966	0.975 and 1.097	0.914	0.137
kk	0.999	1.014	1.014	1.018	0.959 and 1.083	0.898	0.110
hk	1.014	0.998	0.997	1.039	0.919 and 1.043	0.867	0.130
kh	1.051	1.055	1.054	1.056	0.974 and 1.099	0.918	0.136

<sup>a</sup>Reference [26].

<sup>b</sup>Reference [27].

<sup>c</sup>This work.

<sup>d</sup>Reference [18].

Finally, measured coherence times for the NV centers in SiC are significantly smaller than the ones reported for the divacancy [8,9], and the reason for this difference is yet unknown. In particular, it is unclear whether the NV coherence is limited by noise channels other than the interaction with the nuclear spin bath or rather the coupling of the electron spin bath has a different origin for the NV than for the divacancies.

Here we report a set of measurements and first-principles calculations of the ZPL of the NV center in 4H-SiC which show a consistent trend as a function of the defect location in the crystal. Our experimental data are in excellent agreement with those of Ref. [27]. We discuss the dependence of the ZPL values on the details of the geometrical configurations of the defect in the ground and excited states and the resulting sensitivity to strain fields in the host crystal. Our joint theoretical and experimental study reveals a large sensitivity of the spin state of the defect to strain and symmetry. Using hyperfine coupling constants computed from first principles, we predict the coherence times of the NV center and compare our results with recent experiments and with measurements obtained for the divacancy in SiC [10], thus elucidating differences and similarities between the two types of defect centers.

The rest of the paper is organized as follows. In the next section we describe our computational and experimental methods. Our results are discussed in Sec. III and our conclusions given in Sec. IV.

TABLE II. Value (MHz) of the components of the zero field splitting tensor ( $D;E$ ) obtained in this and previous works. The values reported in Refs. [18,27] are the same.

Configuration	Expt. <sup>a</sup>	Expt. <sup>b</sup>	Theor. <sup>c</sup>	Theor. <sup>b</sup>
hh	1331; 0	1339; 0	1427; 0	1513; ~0
kk	1282; 0	1288; 0	1377; 0	1454; 0
hk	1193; 104	1232; 111	1331; 110	1409; 110
kh	1328; 15	1355; 15	1404; 44	1489; 45

<sup>a</sup>References [18,27].

<sup>b</sup>This work.

<sup>c</sup>Reference [18].

## II. METHODS

### A. Computational methods

We carried out calculations of the electronic properties of the NV center in 4H-SiC using DFT with the PBE functional [29]. We used the Quantum ESPRESSO (QE) code [30], a plane-wave basis set with a kinetic energy cutoff of 80 Ry and SG15 optimized norm-conserving Vanderbilt (ONCV) pseudopotentials [31]. As shown in Fig. 1(a), there are four different defect configurations of  $N_C V_{Si}$  in 4H-SiC, depending on the sites where the N atom and vacancy reside: hh and kk, the axial configurations, have  $C_{3v}$  symmetry; hk and kh, the basal configurations, have lower symmetry  $C_{1h}$ . After determining the ground-state electronic structure of all four configurations, we computed the ZPLs using constrained DFT [32], where all geometries were relaxed with a force threshold of 10 meV/Å. We carried out calculations with 256-, 576-, 768-, 1024-, and 2400-atom supercells and the  $\Gamma$  point to sample the supercell Brillouin zone. We used fractional occupation numbers for degenerate states, thus neglecting Jahn-Teller (JT) distortions. However, using the 576-atom cell, we verified that the ordering of ZPLs was not affected by our choice of occupation numbers for the single-particle states, by comparing results

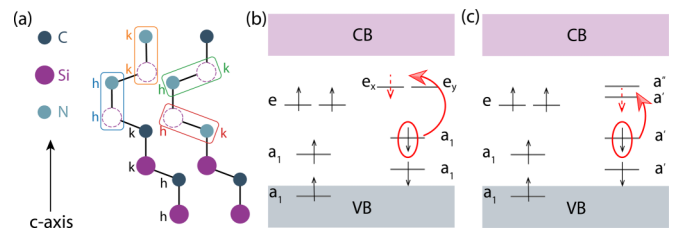


FIG. 1. (a) Four possible configurations of the  $NV^-$  center in 4H-SiC, where N substitutes a C atom and a Si vacancy is present: axial defects are denoted as hh and kk; basal defects are denoted as hk and kh. “h” (quasihexagonal) and “k” (quasicubic) are nonequivalent sites. (b) Electronic structure of the  $N_C V_{Si}$  center in 4H-SiC for axial configurations where defect levels are degenerate due to the  $C_{3v}$  symmetry. (c) Electronic structure of basal configurations where degeneracy of unoccupied levels is lifted due to the lower symmetry  $C_{1h}$ . The black arrows represent electron spins in the ground state whereas the small dashed arrows represent the spin being excited from the circled spin levels.

obtained with fractional and integer occupation numbers (see Table S1 of the Supplemental Material [33]). When using integer occupation numbers JT distortions were taken into account. Overall, we found a systematic 0.4-eV decrease for all four defect configurations when the JT effect is taken into account and no symmetry constraint was applied; this systematic shift did not affect the ordering of the ZPLs of the various configurations.

We computed coherence times from the decay of the density matrix computed with the following spin Hamiltonian:

$$H = \mu_B \mathbf{B} \cdot \mathbf{g} \cdot \mathbf{S} + \sum_N \gamma_N \mathbf{B} \cdot \mathbf{I} + \mathbf{S} \cdot \mathbf{D} \cdot \mathbf{S} + \sum_N \mathbf{S} \cdot \mathbf{A} \cdot \mathbf{I} + \sum_N \mathbf{I} \cdot \mathbf{P} \cdot \mathbf{I}, \quad (1)$$

where  $\mathbf{S}$  is the electron spin and  $\mathbf{I}$  is the nuclear spin. The first two terms describe electron and nuclear Zeeman effects, respectively, when an external magnetic field  $\mathbf{B}$  is applied;  $\mu_B$  is the Bohr magneton and  $\gamma_N$  is the nuclear gyromagnetic ratio of the  $N$ th nucleus. The third term in Eq. (1) is the zero-field splitting (ZFS) term where  $\mathbf{D}$  is the ZFS tensor and one usually defines the components  $D = D_{zz} - \frac{1}{2}(D_{xx} + D_{yy})$  and  $E = \frac{1}{2}(D_{yy} - D_{xx})$ . In the last two terms in Eq. (1),  $\mathbf{A}$  is the hyperfine tensor and  $\mathbf{P}$  is the nuclear quadrupole tensor.

We performed zero-field splitting calculations using the open-source package PyZFS [34], projector-augmented wave (PAW) pseudopotentials [35], and a 576-atom supercell. The hyperfine parameters and the quadrupole tensors were obtained using the GIPAW pseudopotentials with the GIPAW module of QE. We report the results of ZFS in Table II obtained using a 576-atom supercell; the hyperfine and quadrupole tensors computed using the 1024-atom supercell are reported in Table S2 of the Supplemental Material [33]. Although the  $D$  values are known to be sensitive to the supercell size [36], we limited our calculations to 576-atom supercells due to their computational cost. Our results for the  $\mathbf{D}$  tensor are consistent with those of Ref. [18]; however, we did find systematic quantitative differences which may be due to the use of different pseudopotentials [9,37]. Additionally, spin contamination is possibly another source of the overestimation of ZFS, as suggested in Ref. [38]. Our optically detected magnetic resonance (ODMR) measurements are in agreement with previous reports as shown in Table II. As expected from the symmetry of the defects, values of  $E$  of hh and kk are zero, whereas those of hk and kh have finite values. Our quadrupole splitting and hyperfine splitting results are reported in Table S2 of the Supplemental Material [33], and are in agreement with the results of Ref. [39].

Using the DFT-predicted spin Hamiltonian parameters, we then computed the coherence times  $T_2^*$  and  $T_2$ . The time  $T_2^*$  is measured in a free induction decay experiment and can be computed from the decay of the off-diagonal elements of the qubit density matrix  $\rho$ . Assuming that a qubit is prepared in the  $\frac{1}{\sqrt{2}}(|0\rangle + |1\rangle)$  state,  $T_2^*$  is obtained from fitting the normalized off-diagonal element [coherence function  $L(t)$ ] to the compressed exponent  $n$  of the form

$$L(t) = \langle 0 | \rho(t) | 1 \rangle / \langle 0 | \rho(0) | 1 \rangle = e^{-(t/T_2^*)^n}. \quad (2)$$

The coherence time  $T_2$  describes dephasing of the qubit as obtained in a Hahn-echo experiment, in which a  $\pi$  pulse is applied after initialization before the measurement of the qubit state. This  $\pi$  pulse effectively removes the static part of the noise, and thus  $T_2$  depends only on the dynamical fluctuations of the magnetic noise.  $T_2$  is also obtained from fitting the coherence envelope function similar to the expression of Eq. (2).

Here we assume  $T_1$  to be infinitely longer than  $T_2$ ; hence our predictions are valid at low temperatures. Although  $T_1$  of the NV center in SiC is not known and the range of temperatures where our assumption is valid is difficult to estimate, we note that, for example, for the NV center in diamond,  $T_1$  is much longer than  $T_2$  for temperatures lower than 200 K [40]; furthermore,  $T_1$  of the divacancy and other defects in SiC is also longer than  $T_2$  at 2 K [41] or even at room temperature [8,42]. We performed the calculations of coherence times with the cluster correlation expansion (CCE) method for axial centers [43], and with the generalized CCE with Monte Carlo bath state sampling (gCCE) for the basal defects [11]. We used DFT-predicted hyperfine values for nuclear spins within a 1-nm distance from the defect. For larger distances, the hyperfine tensors were approximated with point dipoles. The ensemble-averaged coherence time was obtained by averaging over systems without strongly coupled ( $A_{zz} > 1$  MHz) nuclear spins. The nitrogen spin was assumed to be initialized in the  $m_s = 0$  state.

## B. Experimental methods

A commercially purchased n-type 4H-SiC from Cree Inc. is implanted with  $^{12}\text{C}$  at 190 KeV with a dose of  $10^{13}$  ions/cm<sup>2</sup> and annealed for 900°C for 30 min. The sample is then placed in a closed optical cycle cryostat with microwave access and cooled down to 15 K. A 462-nm multimode laser with 800 mW power illuminated the sample, while the resultant photoluminescence spectra were collected with a liquid-nitrogen-cooled InGaAs photodetector array after passing through a spectrometer. Since most of the resonant frequencies between  $\text{VV}^0$  and  $\text{NV}^-$  are around the same range, a small 26 G field is applied to separate the  $c$ -axis defects from the basal ones. For each microwave frequency scan, two spectra are acquired, one with microwaves and one without. The difference of the two scans for various microwave excitation allows the spectral resolution of magnetic resonance. While the  $c$ -axis defects  $m_s = \pm 1$  levels are split exactly by 73 MHz due to the Zeeman effect, the basal defects remain mostly unchanged, enabling spectral identification of  $c$ -axis and basal defect ZPLs and their corresponding  $D$  and  $E$  values.

## III. RESULTS AND DISCUSSION

### A. Electronic structures and zero-phonon lines

Our results for the ZPLs of the NV center in 4H-SiC are reported in Table I. Figure 2 shows the spectrally resolved ODMR signal with 26 G applied magnetic field which resulted in split ODMR lines as annotated. More detailed ODMR data are shown in Fig. S10 of the Supplemental Material [33].

In order to understand the influence of numerical approximations on our electronic structure calculations, we

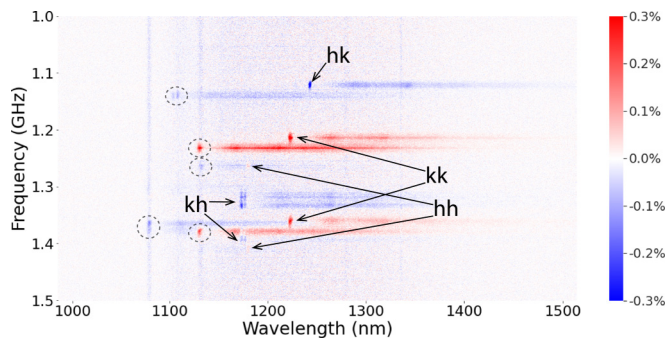


FIG. 2. Spectrally resolved optically detected magnetic resonance (ODMR) spectrum of 4H-SiC with 26 G magnetic field applied along the  $c$  axis. Four NV configurations are denoted with arrows, and dashed circles are from the divacancies contained in the sample. Contrast (in %) is indicated in the scale bar. The frequency-independent contrast is an experimental artifact from the PL change likely due to heating when the microwave is on. The splitting of kh at around 1.33 GHz is likely a split ZPL or a phonon replica.

first compared the fundamental gaps [difference between the highest occupied Kohn-Sham (HOKS) state and the lowest unoccupied Kohn-Sham (LUKS) state] obtained with supercells of different sizes. As shown in Fig. 3(a) fundamental gaps are numerically converged within 0.02 eV only for 2400-atom cells. Although the qualitatively correct spin-triplet electronic structure is obtained with supercells of moderate size (256 atoms), numerically converged band gaps require much larger systems, hinting that also for the calculation of accurate ZPL results, large supercells may be required.

Indeed we found that only when computing ZPLs as a function of several cell sizes, including 2400-atom cells, and then extrapolating our results, the trends observed experimentally for the ZPL of different geometries could be reproduced.

We used the function  $f(x) = a/x^2 + b$ , with  $x$  equal to the number of atoms for the extrapolation shown in Fig. 3(b). In our finite-size scaling, we excluded the 256 atoms for axial configurations and 768 atoms for basal configurations because these supercells are anisotropic. In 256-atom supercells, the defect is much closer to its image in the (0001) plane than in the  $c$ -axis direction, thus further affecting the axial defects; in 768-atom supercells, the cell size is different in the  $[1\bar{1}00]$  and  $[11\bar{2}0]$  directions, artificially lowering the symmetry and thus affecting the results obtained for basal configurations. Note that the ZPL values of the axial configurations, hh and kk, are more sensitive to the choice of the cell size than those of the hk and kh ones. We also note that there is a systematic difference between the calculated values and experimental ones, which we ascribe to the choice of the functional, as PBE is known to underestimate band gaps. However, this systematic difference does not affect the trends as a function of the geometry, which is found to be in good agreement with our experimental results and with those of Ref. [27].

Given the extreme sensitivity of ZPL values to geometrical details, it is interesting to compare the structures of the ground and excited states of the four defect configurations (see Fig. 4 and Figs. S2–S5 in the Supplemental Material [33]). We found that in the axial defects, hh and kk, the three C atoms form equilateral triangles both in the ground and excited states ( $C_{3v}$  point group). In both cases the C-C distance is larger in the excited state (by 0.11 Å) and kk has a larger C-C distance (by 0.13 Å) than the hh configuration. In the basal defects, the three C atoms around the defect form isosceles triangles, and again the C-C distances are elongated relative to the ground state. Interestingly, in the geometry of the excited state of the hk defect the C atoms form an almost equilateral triangle.

We found that in order to converge C-C distances, large supercells are required: the difference of the C-C distances

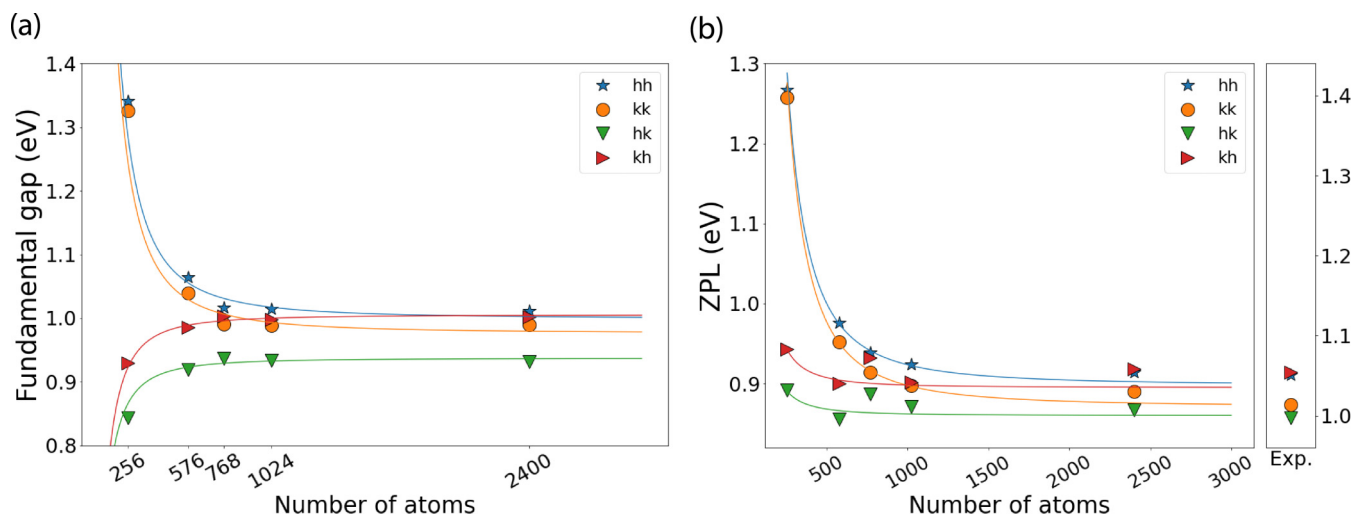


FIG. 3. (a) Computed fundamental band gap of the four different defect configurations of the NV center in 4H-SiC as a function of the supercell size, extrapolated using the function  $f(x) = a/x^2 + b$ . The value obtained for the 256-atom-site supercell was excluded from the fit as an outlier (in this case the cell is highly anisotropic). The fundamental gap was computed as the energy difference of the highest occupied and lowest unoccupied Kohn-Sham eigenvalues. (b) Computed zero-phonon lines (ZPLs) as a function of the supercell size, extrapolated using the function  $f(x) = a/x^2 + b$  (the result obtained with the 256-atom-site supercell was excluded from the fit). Experimental results are shown in the rightmost panel. Note that all calculations are performed by using only the  $\Gamma$  point to sample the supercell Brillouin zone.

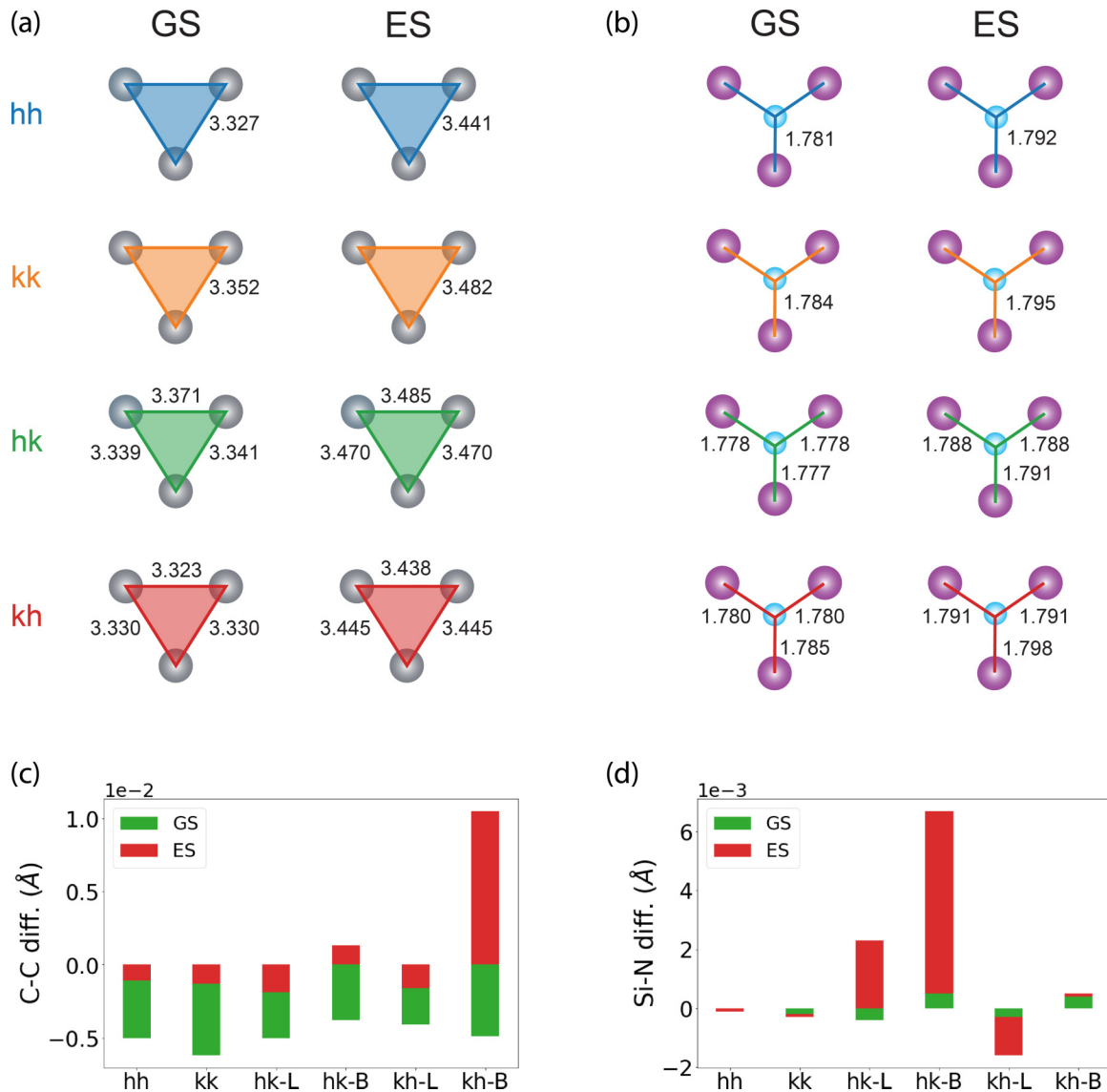


FIG. 4. (a) Computed geometries of carbon atoms (gray spheres) surrounding the Si vacancy of the NV center in 4H-SiC. We show results obtained with a 1024-atom-site supercell for the four different defect configurations, for both ground-state (GS) and excited-state (ES) configurations. The C-C distances are given in Å. The three C atoms in the axial configurations (hh and kk) form an equilateral triangle. The three C atoms in the basal configurations (hk and kh) form an isosceles triangle. (b) Computed geometries of the Si atoms (purple spheres) surrounding the N atom (blue sphere), with bond lengths indicated in Å. (c) Difference between C-C distances computed with a 1024- and 256-atom supercells. (d) Difference between the Si-N bond lengths computed with a 1024- and 256-atom supercell. On the abscissa, “-L” indicates the two equal sides in the isosceles triangle and “-B” indicates the third side.

obtained with 256- and 1024-atom-site supercells can be as large as 0.01 Å (e.g., for the kh defect in the excited state). Importantly, the changes in the C-C and Si-N distances as a function of cell size are different for the four configurations and that is the reason why full convergence must be attained for all configurations in order to meaningfully compare results with experiment.

The slight geometrical differences between the various defect configurations are also reflected in the single-particle wavefunctions localized at the defect site. In Fig. 5 we compare the wavefunctions of the hh defect computed with the 576-atom and the 1024-atom supercells. Note that the localization of the wavefunctions is sensitive to the chosen supercell size, while the  $C_{3v}$  symmetry is preserved in both

supercells, as expected. This trend was not only observed for the hh defect, but also for the other configurations (see Fig. S6 of the Supplemental Material [33]).

Our results on the sensitivity of ZPL values to details of the SiC structure point at an important physical effect: the NV center in SiC is extremely sensitive to strain fields in the host crystal, and hence it appears to be a good candidate as a strain sensor.

### B. Spin Hamiltonian parameters and coherence times

We now turn to discussing coherence times of the NV in 4H-SiC. One of the advantages of SiC-based qubits compared to diamond spin qubits is the presence of the binary lattice,

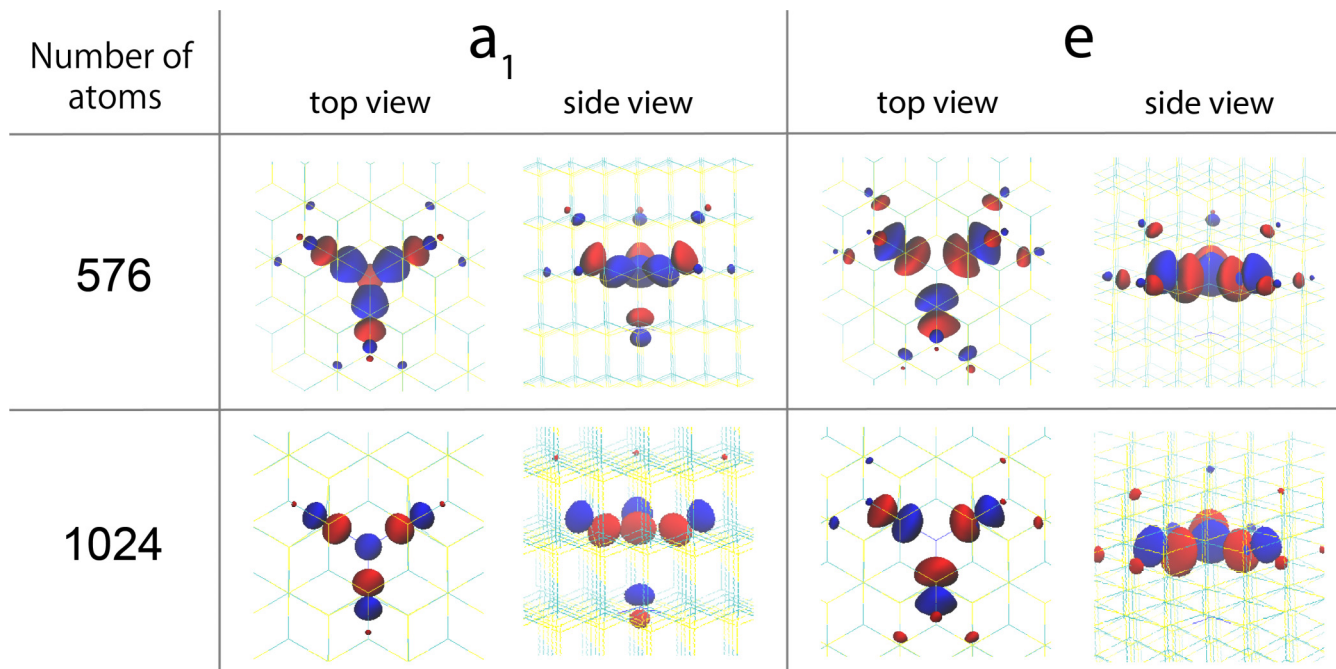


FIG. 5. Isosurfaces of the single-particle orbitals of the  $a_1$  and  $e$  states of the NV center in 4H-SiC at isovalue of  $\pm 0.002$  for the hh configuration obtained in supercells with 576 and 1024 atoms. Red and blue isosurfaces indicate positive and negative values, respectively.

which leads to a significant enhancement of the coherence time of divacancies in SiC even at the natural isotopic concentration of nuclear spins [9,10]. We show below that axial NV centers in SiC exhibit the same coherence properties as the VV in SiC and that the theoretical limit of  $T_2$  is similar to that of the axial divacancy (Table III).

As mentioned earlier, compared to axial NV centers, basal configurations exhibit a lower symmetry and hence a substantial transverse zero-field splitting  $E$ . The lower symmetry allows for clock transitions to emerge at zero applied magnetic field. The frequency of clock transitions is insensitive to the magnetic field fluctuations up to first order [44], thus significantly improving protection from the nuclear spin noise.

Our calculations predict a substantially larger  $T_2^*$  for the basal NV centers at zero magnetic field compared to that of

the axial ones. We note the importance of the amplitude of the transverse ZFS in determining the value of  $T_2^*$  at clock transitions. The coherence times for the kh NV center at zero magnetic field, computed using the theoretical value of the ZFS, is larger than the one obtained with the experimental  $E$  value by a factor of 2. This significant difference points at the necessity (Table II) of accurate predictions of spin Hamiltonian parameters [45].

Finally, we investigated the dependence of the Hahn-echo coherence time  $T_2$  on the magnetic field ( $B_z$ ), shown in Fig. 6 computed using measured  $E$  values [18,27]. At low magnetic fields the hyperfine couplings are stronger or on par with the energy splitting arising from the external magnetic field. The increase of the magnetic field leads to an increase in the speed of precession of single nuclear spins, which in

TABLE III. Nuclear spin bath-limited coherence time. For the kh configuration, we show coherence times computed using both the experimental [18,27] and our theoretical value of the  $E$  component of the zero field splitting tensor (see Table II). The experimental data for the kk divacancy (kk-VV) are from Refs [8–10]. For the axial NV centers the coherence time is computed at magnetic field of 200 G and for the basal centers at zero applied magnetic field.

Configuration	$T_2^*$ ( $\mu$ s)	$T_2$ (ms)
hh	0.64 (1.0 <sup>a</sup> )	1.32 (0.0171 <sup>a</sup> )
kk	0.85 (0.4 <sup>b</sup> )	1.31
hk	520	2.2
kh (expt. $E$ )	150	0.99
kh (theor. $E$ )	340	1.68
kk-VV	1.1	1.2

<sup>a</sup>RT measurement from [24].

<sup>b</sup>Low temperature measurement from [23].

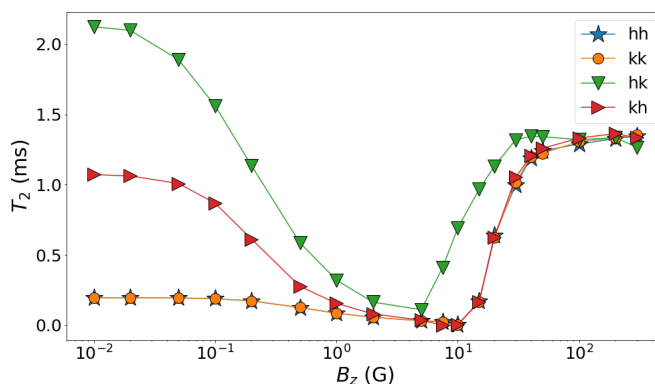


FIG. 6. Computed coherence time  $T_2$  as a function of the strength of the applied magnetic field ( $B_z$ ) for four configurations of the NV center in 4H-SiC. Note that the  $T_2$  of the hh and kk configurations is similar, especially in the lower  $B_z$  range.

turn leads to faster fluctuations of the magnetic noise and to a decrease in coherence time in this regime. For the basal defects with clock transition, the decrease in coherence time is further exacerbated by the removal of the qubit energy levels from the avoided crossing, at which the additional protection from the magnetic noise is achieved [46]. We note that the clock transition in basal configurations leads to a substantial increase in  $T_2$  at  $B_z = 0$ , relative to that of axial configurations. At strong magnetic fields all configurations exhibit the same coherence time of  $\sim 1.3$  ms as the Zeeman splitting plays a major role in this regime, leading to only secular pairwise nuclear spin flips being allowed and thus to an increase of  $T_2$  in this regime. For the hk case at natural abundance of nuclear spins, the predicted Hahn-echo coherence time at zero field is similar to those of the divacancies in isotopically purified SiC [10]. Furthermore, the high amplitude of the transverse ZFS affects the coherence time also for intermediate values of the magnetic fields ( $B_z = 10\text{--}50$  G): interestingly, we found that the  $T_2$  of the hk NV center is higher than those of other NV and divacancy configurations.

#### IV. CONCLUSIONS

In summary, using first-principles calculations and spectrally resolved ODMR measurements, we investigated the properties of the NV center in SiC, which were found to be extremely sensitive to strain fields present in the host SiC crystal. Our theoretical and experimental results consistently predict

the same trend of the ZPL as a function of the geometrical configuration of the defect, in agreement with independent measurements recently reported in the literature [27]. We ascribe previous disagreements between theory and experiment to the use of moderately sized supercells, which we showed are insufficient to obtain numerically accurate predictions. We also predicted coherence times of the NV in basal and axial configurations and found a substantially larger  $T_2^*$  of the basal NV centers at zero magnetic field, compared to that of the axial configurations. Interestingly our calculations show that at natural nuclear spin abundance the Hahn-echo coherence time at zero field of one of the basal configurations is similar to that of the divacancies in isotopically purified SiC. Given the readily accessible  $^{14}\text{N}$  nuclear registers and the availability of universal dressing schemes at clock transitions [47] to protect qubit states, we expect the basal NV centers to provide robust platforms for the next generation of defect qubits in SiC.

#### ACKNOWLEDGMENTS

This work was supported by Grant No. AFOSRFA9550-19-1-0358 and made use of computational resources provided by the University of Chicago's Research Computing Center and the National Energy Research Scientific Computing Center (NERSC). Experiment efforts (B.K., D.A.) were supported by the U.S. Department of Energy, Office of Science, Basic Energy Sciences, Materials Sciences and Engineering Division. We acknowledge helpful discussions with Dr. Meng Ye, Dr. He Ma, Dr. Wennie Wang, Yu Jin, Dr. Uwe Gerstmann, and Dr. Gary Wolfowicz.

- 
- [1] G. Wolfowicz, F. J. Heremans, C. P. Anderson, S. Kanai, H. Seo, A. Gali, G. Galli, and D. D. Awschalom, Quantum guidelines for solid-state spin defects, *Nat. Rev. Mater.* (2021), doi: [10.1038/s41578-021-00306-y](https://doi.org/10.1038/s41578-021-00306-y).
  - [2] N. T. Son, C. P. Anderson, A. Bourassa, K. C. Miao, C. Babin, M. Widmann, M. Niethammer, J. Ul Hassan, N. Morioka, I. G. Ivanov *et al.*, Developing silicon carbide for quantum spintronics, *Appl. Phys. Lett.* **116**, 190501 (2020).
  - [3] J. R. Weber, W. F. Koehl, J. B. Varley, A. Janotti, B. B. Buckley, C. G. Van de Walle, and D. D. Awschalom, Quantum computing with defects, *Proc. Natl. Acad. Sci. USA* **107**, 8513 (2010).
  - [4] E. Herbschleb, H. Kato, Y. Maruyama, T. Danjo, T. Makino, S. Yamasaki, I. Ohki, K. Hayashi, H. Morishita, M. Fujiwara *et al.*, Ultra-long coherence times amongst room-temperature solid-state spins, *Nat. Commun.* **10**, 3766 (2019).
  - [5] M. W. Doherty, N. B. Manson, P. Delaney, F. Jelezko, J. Wrachtrup, and L. C. Hollenberg, The nitrogen-vacancy colour centre in diamond, *Phys. Rep.* **528**, 1 (2013).
  - [6] R. Schirhagl, K. Chang, M. Loretz, and C. L. Degen, Nitrogen-vacancy centers in diamond: Nanoscale sensors for physics and biology, *Annu. Rev. Phys. Chem.* **65**, 83 (2014).
  - [7] D. D. Awschalom, R. Hanson, J. Wrachtrup, and B. B. Zhou, Quantum technologies with optically interfaced solid-state spins, *Nat. Photonics* **12**, 516 (2018).
  - [8] W. F. Koehl, B. B. Buckley, F. J. Heremans, G. Calusine, and D. D. Awschalom, Room temperature coherent control of defect spin qubits in silicon carbide, *Nature (London)* **479**, 84 (2011).
  - [9] H. Seo, A. L. Falk, P. V. Klimov, K. C. Miao, G. Galli, and D. D. Awschalom, Quantum decoherence dynamics of divacancy spins in silicon carbide, *Nat. Commun.* **7**, 12935 (2016).
  - [10] A. Bourassa, C. P. Anderson, K. C. Miao, M. Onizhuk, H. Ma, A. L. Crook, H. Abe, J. Ul-Hassan, T. Ohshima, N. T. Son, G. Galli, and D. D. Awschalom, Entanglement and control of single nuclear spins in isotopically engineered silicon carbide, *Nat. Mater.* **19**, 1319 (2020).
  - [11] M. Onizhuk, K. C. Miao, J. P. Blanton, H. Ma, C. P. Anderson, A. Bourassa, D. D. Awschalom, and G. Galli, Probing the coherence of solid-state qubits at avoided crossings, *PRX Quantum* **2**, 010311 (2021).
  - [12] D. J. Christle, A. L. Falk, P. Andrich, P. V. Klimov, J. U. Hassan, N. T. Son, E. Janzén, T. Ohshima, and D. D. Awschalom, Isolated electron spins in silicon carbide with millisecond coherence times, *Nat. Mater.* **14**, 160 (2015).
  - [13] H. J. von Bardeleben, J. L. Cantin, E. Rauls, and U. Gerstmann, Identification and magneto-optical properties of the NV center in 4H-SiC, *Phys. Rev. B* **92**, 064104 (2015).
  - [14] G. Cheng, Y. Wan, and S. Yan, Optical and spin coherence properties of NV center in diamond and 3C-SiC, *Comput. Mater. Sci.* **154**, 60 (2018).
  - [15] L. Gordon, A. Janotti, and C. G. Van de Walle, Defects as qubits in 3C- and 4H-SiC, *Phys. Rev. B* **92**, 045208 (2015).

- [16] S. A. Zargaleh, S. Hameau, B. Eble, F. Margaillan, H. J. von Bardeleben, J. L. Cantin, and W. Gao, Nitrogen vacancy center in cubic silicon carbide: A promising qubit in the 1.5  $\mu\text{m}$  spectral range for photonic quantum networks, *Phys. Rev. B* **98**, 165203 (2018).
- [17] H. J. von Bardeleben, J. L. Cantin, A. Cs r , A. Gali, E. Rauls, and U. Gerstmann, NV centers in 3C, 4H, and 6H silicon carbide: A variable platform for solid-state qubits and nanosensors, *Phys. Rev. B* **94**, 121202(R) (2016).
- [18] A. Cs r , H. J. von Bardeleben, J. L. Cantin, and A. Gali, Characterization and formation of NV centers in 3C, 4H, and 6H SiC: An *ab initio* study, *Phys. Rev. B* **96**, 085204 (2017).
- [19] J. Meijer, B. Burchard, M. Domhan, C. Wittmann, T. Gaebel, I. Popa, F. Jelezko, and J. Wrachtrup, Generation of single color centers by focused nitrogen implantation, *Appl. Phys. Lett.* **87**, 261909 (2005).
- [20] J. Rabeau, P. Reichart, G. Tamanyan, D. Jamieson, S. Prawer, F. Jelezko, T. Gaebel, I. Popa, M. Domhan, and J. Wrachtrup, Implantation of labelled single nitrogen vacancy centers in diamond using  $\text{N}_{15}$ , *Appl. Phys. Lett.* **88**, 023113 (2006).
- [21] K. Ohno, F. J. Heremans, C. F. de las Casas, B. A. Myers, B. J. Alem n, A. C. Bleszynski Jayich, and D. D. Awschalom, Three-dimensional localization of spins in diamond using 12C implantation, *Appl. Phys. Lett.* **105**, 052406 (2014).
- [22] S. B. van Dam, M. Walsh, M. J. Degen, E. Bersin, S. L. Mouradian, A. Galiullin, M. Ruf, M. IJspeert, T. H. Tamini , R. Hanson, and D. R. Englund, Optical coherence of diamond nitrogen-vacancy centers formed by ion implantation and annealing, *Phys. Rev. B* **99**, 161203(R) (2019).
- [23] Z. Mu, S. A. Zargaleh, H. J. von Bardeleben, J. E. Fr ch, M. Nonahal, H. Cai, X. Yang, J. Yang, X. Li, I. Aharonovich, and W. Gao, Coherent manipulation with resonant excitation and single emitter creation of nitrogen vacancy centers in 4H silicon carbide, *Nano Lett.* **20**, 6142 (2020).
- [24] J.-F. Wang, F.-F. Yan, Q. Li, Z.-H. Liu, H. Liu, G.-P. Guo, L.-P. Guo, X. Zhou, J.-M. Cui, J. Wang, Z.-Q. Zhou, X.-Y. Xu, J.-S. Xu, C.-F. Li, and G.-C. Guo, Coherent Control of Nitrogen-Vacancy Center Spins in Silicon Carbide at Room Temperature, *Phys. Rev. Lett.* **124**, 223601 (2020).
- [25] J.-F. Wang, Z.-H. Liu, F.-F. Yan, Q. Li, X.-G. Yang, L. Guo, X. Zhou, W. Huang, J.-S. Xu, C.-F. Li, and G.-C. Guo, Experimental optical properties of single nitrogen vacancy centers in silicon carbide at room temperature, *ACS Photonics* **7**, 1611 (2020).
- [26] S. A. Zargaleh, B. Eble, S. Hameau, J.-L. Cantin, L. Legrand, M. Bernard, F. Margaillan, J.-S. Lauret, J.-F. Roch, H. J. von Bardeleben, E. Rauls, U. Gerstmann, and F. Treussart, Evidence for near-infrared photoluminescence of nitrogen vacancy centers in 4H-SiC, *Phys. Rev. B* **94**, 060102(R) (2016).
- [27] S. A. Zargaleh, H. J. von Bardeleben, J. L. Cantin, U. Gerstmann, S. Hameau, B. Ebl , and W. Gao, Electron paramagnetic resonance tagged high-resolution excitation spectroscopy of NV-centers in 4H-SiC, *Phys. Rev. B* **98**, 214113 (2018).
- [28] K. Khazen, H. J. von Bardeleben, S. A. Zargaleh, J. L. Cantin, M. Zhao, W. Gao, T. Biktagirow, and U. Gerstmann, High-resolution resonant excitation of NV centers in 6H-SiC: A matrix for quantum technology applications, *Phys. Rev. B* **100**, 205202 (2019).
- [29] J. P. Perdew, K. Burke, and M. Ernzerhof, Generalized Gradient Approximation Made Simple, *Phys. Rev. Lett.* **77**, 3865 (1996).
- [30] P. Giannozzi, S. Baroni, N. Bonini, M. Calandra, R. Car, C. Cavazzoni, D. Ceresoli, G. L. Chiarotti, M. Cococcioni, I. Dabo *et al.*, QUANTUM ESPRESSO: A modular and open-source software project for quantum simulations of materials, *J. Phys.: Condens. Matter* **21**, 395502 (2009).
- [31] M. Schlipf and F. Gygi, Optimization algorithm for the generation of ONCV pseudopotentials, *Comput. Phys. Commun.* **196**, 36 (2015).
- [32] A. Gali, E. Janz n, P. De k, G. Kresse, and E. Kaxiras, Theory of Spin-Conserving Excitation of the  $\text{N-V}^-$  Center in Diamond, *Phys. Rev. Lett.* **103**, 186404 (2009).
- [33] See Supplemental Material at <http://link.aps.org/supplemental/10.1103/PhysRevMaterials.5.074602> for more spin Hamiltonian parameters results, more detailed analysis of JT effect on zero-phonon lines, defect geometry analysis, and spectrally resolved ODMR results.
- [34] H. Ma, M. Govoni, and G. Galli, PyZFS: A PYTHON package for first-principles calculations of zero-field splitting tensors, *J. Open Source Software* **5**, 2160 (2020).
- [35] A. Dal Corso, Pseudopotentials periodic table: From H to Pu, *Comput. Mater. Sci.* **95**, 337 (2014).
- [36] S. J. Whiteley, G. Wolfowicz, C. P. Anderson, A. Bourassa, H. Ma, M. Ye, G. Koolstra, K. J. Satzinger, M. V. Holt, F. J. Heremans *et al.*, Spin-phonon interactions in silicon carbide addressed by Gaussian acoustics, *Nat. Phys.* **15**, 490 (2019).
- [37] T. Biktagirow, W. G. Schmidt, and U. Gerstmann, Calculation of spin-spin zero-field splitting within periodic boundary conditions: Towards all-electron accuracy, *Phys. Rev. B* **97**, 115135 (2018).
- [38] T. Biktagirow, W. G. Schmidt, and U. Gerstmann, Spin decontamination for magnetic dipolar coupling calculations: Application to high-spin molecules and solid-state spin qubits, *Phys. Rev. Research* **2**, 022024(R) (2020).
- [39] F. F. Murzakhonov, B. V. Yavkin, G. V. Mamin, S. B. Orlinskii, H. J. von Bardeleben, T. Biktagirow, U. Gerstmann, and V. A. Soltamov, Hyperfine and nuclear quadrupole splitting of the  $\text{NV}^-$  ground state in 4H-SiC, *Phys. Rev. B* **103**, 245203 (2021).
- [40] A. Jarmola, V. M. Acosta, K. Jensen, S. Chemerisov, and D. Budker, Temperature- and Magnetic-Field-Dependent Longitudinal Spin Relaxation in Nitrogen-Vacancy Ensembles in Diamond, *Phys. Rev. Lett.* **108**, 197601 (2012).
- [41] C. M. Gilardoni, T. Bosma, D. van Hien, F. Hendriks, B. Magnusson, A. Ellison, I. G. Ivanov, N. Son, and C. H. van der Wal, Spin-relaxation times exceeding seconds for color centers with strong spin-orbit coupling in SiC, *New J. Phys.* **22**, 103051 (2020).
- [42] M. Widmann, S.-Y. Lee, T. Rendler, N. T. Son, H. Fedder, S. Paik, L.-P. Yang, N. Zhao, S. Yang, I. Booker *et al.*, Coherent control of single spins in silicon carbide at room temperature, *Nat. Mater.* **14**, 164 (2015).
- [43] W. Yang and R.-B. Liu, Quantum many-body theory of qubit decoherence in a finite-size spin bath, *Phys. Rev. B* **78**, 085315 (2008).

- [44] K. C. Miao, A. Bourassa, C. P. Anderson, S. J. Whiteley, A. L. Crook, S. L. Bayliss, G. Wolfowicz, G. Thiering, P. Udvarhelyi, V. Ivády, H. Abe, T. Ohshima, Á. Gali, and D. D. Awschalom, Electrically driven optical interferometry with spins in silicon carbide, *Sci. Adv.* **5**, eaay0527 (2019).
- [45] K. Ghosh, H. Ma, M. Onizhuk, V. Gavini, and G. Galli, Spin-spin interactions in solids from mixed all-electron and pseudopotential calculations—a path to screening materials for spin qubits, [arXiv:2102.00162](https://arxiv.org/abs/2102.00162) [npj Computational Materials (to be published)].
- [46] N. Zhao, S.-W. Ho, and R.-B. Liu, Decoherence and dynamical decoupling control of nitrogen vacancy center electron spins in nuclear spin baths, *Phys. Rev. B* **85**, 115303 (2012).
- [47] K. C. Miao, J. P. Blanton, C. P. Anderson, A. Bourassa, A. L. Crook, G. Wolfowicz, H. Abe, T. Ohshima, and D. D. Awschalom, Universal coherence protection in a solid-state spin qubit, *Science* **369**, 1493 (2020).

*Correction:* A minor typographical error in Eq. (2) has been fixed.